Raman spectroscopy under tensile strain on kagome FeSn crystal

Sharon S. Philip,[1] Yu Tao[@],[1] Bishal Thapa,[2] Igor I. Mazin,[2] and Despina Louca[1,*]

[1] *Department of Physics, University of Virginia, Charlottesville, Virginia 22904, USA*
[2] *Physics and Astronomy Department, George Mason University, Fairfax, VA 22030, USA*

Raman spectroscopy coupled with first principle calculations were performed on the antiferromagnetic kagome metal FeSn to investigate the effects of strain. The single crystals were measured in free form and under strain, applied by bending a flexible substrate at room temperature. Several Raman modes were observed, with or without strain, in addition to the Raman-active E_{2g}, that could not be explained by the P6/mmm crystal symmetry. Under strain, the E_{2g} central peak intensity drops sharply, while the satellite peaks redshift to lower frequencies. Internal strain or leakage of zone-center Raman-forbidden modes were excluded as the origin of these satellites. The satellite peak intensities are comparable to the central mode and cannot be explained by minute impurities in the crystals.

I. INTRODUCTION

Quantum materials host exotic quasiparticles and unconventional states. The underlying quantum effects are dictated by the intricate interactions resulting from strong correlations and entanglement [1–3]. Research on quantum materials has grown rapidly over the past decade and their electronic and magnetic properties have been widely explored [1, 4]. One particularly interesting feature that has attracted much attention recently is the presence of dispersionless flat bands, which arise from strong localization of electrons due to the lattice geometry. The resulting electronic bands appear nearly horizontal with very narrow bandwidths [5–8]. Such lattice-borne flat bands are often associated with nontrivial topologies if combined with spin-orbit coupling [8–10].

Flat bands are analogous to Landau levels observed in the fractional quantum Hall effect (FQHE), the latter created by the degeneracy within the flat Landau levels for particles in large external magnetic fields [11, 12]. Flat bands are found in the midst of dispersive bands, often touching at specific points in momentum space, and can be isolated by breaking time-reversal symmetry (TRS) that creates a gap. In the presence of TRS, flat bands can have a non-zero Chern number due to the presence of a non-trivial Berry phase and such materials can host FQHE in the absence of a strong magnetic field [11, 13, 14]. Material candidates with flat bands are twisted graphene, kagome lattices and heavy fermion compounds [5, 7, 8, 15].

Kagome lattice materials with the corner-sharing triangle geometry, are ideal hosts of frustrated, correlated and topological quantum electronic states. One widely-studied example of this class of materials is $Co_3Sn_2S_2$, which is reported to be a ferromagnetic Weyl semimetal with a giant anomalous Hall effect [16]. In the ferromagnetic Fe_3Sn_2 compound, angle-resolved photoemission spectroscopy (ARPES) measurements along the Γ-K and Γ-M lines demonstrated the presence of a nearly dispersionless flat band at ~ 0.2 eV below the Fermi level [5]. In the antiferromagnetic FeSn, coexistence of bulk Dirac fermions and flat bands have been reported using ARPES as well [17].

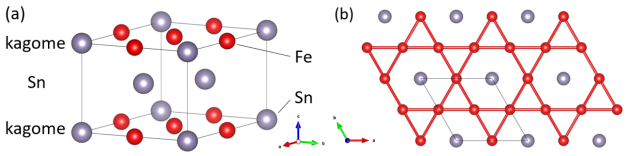

Figure 1. (a) The crystal structure of FeSn, consisting of kagome layers of Fe_3Sn and layers of Sn stacked along the *c*-axis. (b) The kagome layer in the *ab*-plane.

The crystal structure of FeSn is shown in Fig. 1. The Fe atoms are arranged in two-dimensional kagome sheets with Sn atoms sitting at the center of each hexagon (Fig. 1(a)). These kagome layers with Fe_3Sn stoichiometry alternate along the *c*-axis with layers consisting of purely Sn atoms (Fig. 1(b)). FeSn is a layered antiferromagnet with a Neel transition temperature $T_N = 365$ K, where the Fe atoms order ferromagnetically within the kagome layer and antiferromagnetically across layers.

The structure and magnetic properties of FeSn are similarly rich. We previously observed that the spin waves in FeSn persist to temperatures well above T_N, in the paramagnetic state [18]. This was accompanied by an unusual *c*-axis lattice constant anomaly that indicated magneto-elastic coupling. A large electron-magnon interaction was also reported in FeSn at 5 K, that resulted in strong damping of the high energy magnon spectra [19, 20]. From powder inelastic neutron scattering experiments on FeSn, a phonon softening behavior was observed across T_N suggesting spin-phonon coupling [18]. To further explore the elastic properties of FeSn, experiments were performed under uniaxial strain in the antiferromagnetic state. The application of elastic strain is an effective way to modify the lattice structure and bonds that could lead to possible symmetry breaking. Triangular lattice material Mn_3Sn is one such example, known for its highly unusual magneto-elastic and

* Corresponding author; louca@virginia.edu

magnetostriction properties [21–23]. The giant anomalous Hall and thermal Hall effects observed in Mn_3Sn were reported to be sensitive to strain [22, 24]. Elastic strain can also affect other properties in kagome lattice materials. The superconducting transition temperatures of kagome superconductors KV_3Sb_5 and CsV_3Sb_5 can be enhanced under strain [25]. In this work, Raman spectroscopy was used to probe the strain induced effects on the local symmetry of FeSn. Density functional theory (DFT) calculations were used to probe into the phonon modes and investigate the magneto-phonon coupling in FeSn.

II. EXPERIMENTAL AND CALCULATION DETAILS

Single crystals of FeSn were grown using the chemical vapor transport (CVT) method, with I_2 as the transport agent. First, high-purity Fe and Sn metal pieces were loaded in a quartz tube in a molar ratio of 1:1. The materials were sealed in vacuum with 4 mg/cm^{-3} I_2. The 15-cm long ampoule was then inserted horizontally in a tube furnace at 680 °C (sink), with the material side (source) close to the edge of the furnace, allowing a natural temperature gradient. Thin plate-like, hexagonal single crystals were obtained, with a typical growth duration of 1 week.

A single crystal piece was attached to the surface of a PET (Polyethylene terephthalate) substrate using ultrahigh-strength two-component epoxy glue (UHU). The epoxy glue was subsequently cured at 80°C for 1 hour. The sample and the substrate were well electrically isolated because the epoxy glue is an excellent insulator and ensures an effective transfer of strain. Raman spectroscopy measurements were performed using a Renishaw InVia™ Confocal Raman microscope with 1-micron mapping spatial resolution. A 50x L objective lens (0.9 NA) was used to focus the laser and collect the Raman scattered light, and a 3000 lines/mm grating was chosen for spectra acquisition. A 405 nm diode laser was selected for the measurements that offered the best balance between scattering efficiency, fluorescence fluence, and detector efficiency.

The structural and magnetic calculations of FeSn were performed using the Vienna ab initio simulation package (VASP)[26–28] and analyzed with the aid of the ISOTROPY software suite [29, 30]. The projector augmented wave (PAW)[31] potentials with the generalized gradient approximation (GGA) exchange-correlation potential in the Perdew–Burke–Ernzerhof[32] version were used in all calculations. The energy cutoff in VASP was $E_{cutoff} \approx 500$ eV and $18 \times 18 \times 11$ k-point sampling was used in the calculations. In order to investigate the effect of magnetism on the phonon spectra, we performed the calculations in a locally nonmagnetic case (local magnetization on Fe fully suppressed), ferromagnetic, and A-type antiferromagnetic (ferromagnetic planes stacked antiferromagnetically). The atomic positions of FeSn were determined with lattice parameters $a = b = 5.289(1)$ Å and $c = 4.461(1)$ Å. We used this optimized structure to calculate the phonon mode for the nonmagnetic (NM) and ferromagnetic (FM) pattern, which contains 6 atoms per unit cell. Meanwhile, the antiferromagnetic (AFM) pattern involves doubling of the unit cell dimensions, resulting in $c = 8.923(1)$ Å and a total of 12 atoms per unit cell. Other internal degrees of freedom converged with an energy cutoff of approximately 500 eV and a k-sample point mesh size of $18 \times 18 \times 11$, with all forces smaller than 0.001 eV/Å. In the NM pattern, there is no net magnetic moment. In the FM pattern, the magnetic moment of Fe is suppressed, while in the AFM pattern, Fe atoms in different planes exhibit opposite magnetic moments. The crystal structure details are tabulated in Table I for the magneto-phonon calculation along with the application of volume conserving unilateral strain.

Magnetic Pattern	Wyckoff Position		Space Group
Element Site			
NM/FM/AFM	Fe	f	191, P6/mmm
	Sn	d	
	Sn	a	
Unilateral Strain			
AFM	Fe	b	65, Cmmm
	Fe	e	
	Sn	j	
	Sn	a	

Table I. Crystallographic Information for Different Magnetic Patterns: NonMagnetic (NM), Ferromagnetic (FM) and Antiferromagnetic (AFM), with Corresponding Wyckoff Positions and Space Groups.

III. RESULTS AND DISCUSSION

A. Raman spectroscopy under strain

The results from the Raman spectroscopy measurements on single crystals of FeSn with and without strain are shown in Fig. 2. All measurements were done at room temperature. The Raman spectrum from a free crystal sample showed four peaks located at 136.42, 155.00, 177.05 and 207.66 cm^{-1} Raman shifts (Fig. 2(a)). The crystal used for this measurement is shown in the inset of Fig. 2(a). The first three peaks were clearly present in all crystals measured, however the peak at 207.66 cm^{-1} had relatively lower intensity and was not discernible in all the crystals measured. This could be due to small differences in sample orientation or thickness. Raman peaks with Stokes shifts smaller than 100 cm^{-1} were below the detection limit of our spectrometer. No Raman peaks with Stokes shifts larger than 250 cm^{-1} were detected either and thus we limit the investigation to

this range. The central peak at 155.00 cm^{-1} is identified to be the E_{2g} mode based on symmetry. However, the additional peaks cannot be deduced from symmetry arguments. Possible sources of the extra Raman peaks might include a phase transition or structural disorder that breaks inversion symmetry leading to extra peaks. Thus, not only the q = 0 phonon modes contribute to the Raman spectra [33]. Similarly, q ≠ 0 phonon center modes might arise from stacking or impurities, although no second phases were detected in the crystals. Our earlier neutron scattering measurements revealed no new crystal symmetry from the crystal structure refinement either [18]. Similarly, the local atomic structure obtained from Fourier transforming the structure function showed no evidence of new, short-range order. The origin of the satellites is quite puzzling at present.

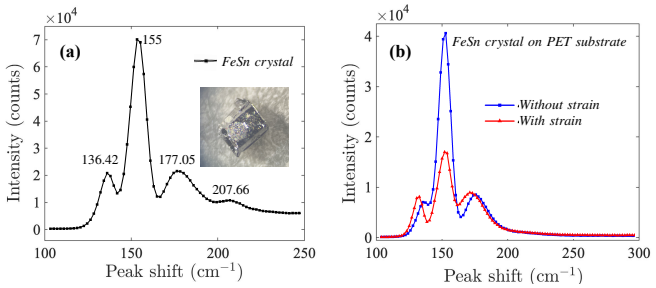

Figure 2. The Raman spectroscopic results on single crystal sample of FeSn using 405 nm laser excitation is shown. (a) The measurement on a free crystal sample. The image of the measured sample is shown on the inset. (b) A comparison of FeSn crystal on a PET substrate with and without strain.

Shown in Fig. 2(b) is the Raman spectra of a crystal attached to a PET substrate revealing the effect of applied tensile strain. First we note that the spectra with and without PET are quite similar. With applied strain, the intensity of the E_{2g} mode (155.00 cm^{-1}) drops significantly. Such a drastic drop of the central Raman mode indicates a change in the polarizability and in the electron-phonon coupling. The intensity drop is accompanied by a -1cm^{-1} redshift. At the same time, the satellite peaks show a larger redshift under strain. While the peaks at 136.42 and 177.05 cm^{-1} show smaller changes in intensity, notably, under strain, these peaks exhibit a modest increase in intensity and a distinct energy redshift. Under tensile strain, the peaks appear at 131.69 and 172.01 cm^{-1}, with peak shifts by 3.92 cm^{-1} and 3.5 cm^{-1}, respectively. Although the origin of these peaks is not understood at present, such a shift would indicate a change in the bond lengths, i.e. when the bond lengths become longer as expected during tensile strain. The reason for this shift is explored further in the next section.

B. Density Functional Theory Calculations

We systematically investigated the magneto-phonon coupling in the FeSn sample by introducing magnetic interactions within the unit cell. First, we performed calculations in the full P6/mmm (#191) group. The crystal structure involves Fe in the 3f Wyckoff position, a coplanar Sn 1a, and a pure Sn layer with the 2d positions. Only one doubly-degenerate Raman-active mode is allowed, E_{2g}, which involves only lateral displacements of the 2d Sn shown in Fig. 3(c). Note that the antiferromagnetic case requires doubling of the unit cell along c. This normally leads to zone-boundary modes with $\mathbf{q} = (0, 0, \pi/c)$ to be tagged as zone-center, even though they remain Raman-forbidden (unless magnetic ordering is accompanied by a charge order). These zone center modes are listed in Table II.

The doubly degenerate E_{2g} mode is the only Raman-active mode allowed by symmetry. The calculated value of 156.6 cm^{-1} is in good agreement with the central peak observed in the experiment at 155.0 cm^{-1}. Interestingly, accounting for the proper magnetic order reduces the computational error by a factor of two. However, we did not observe any evidence for the satellite peaks at 136.42 and 177.05 cm^{-1}. Even assuming possible leakage of non-Raman-active modes, we observe that no optical phonons at $\mathbf{q} = (0, 0, 0)$ or $\mathbf{q} = (0, 0, \pi/c)$ are potential

Optical-Mode				
S. No.	Symmetry	Non Magnetic	Ferro Magnetic	Antiferro Magnetic
1	E_{1u}	213.9	254.4	246.9
2	A_{2u}	223.8	244.6	248.2
	E_{1u}			244.7
	B_{1u}			238.8
	E_{2u}			238.2
	B_{2u}			232.7
3	B_{2u}	150.4	239.6	230.0
4	B_{1u}	194.4	191.8	202.1
5	E_{2u}	137.2	183.7	200.5
	A_{2u}			194.9
	A_{1g}			160.5
6	E_{1u}	131.6	164.2	157.5
7	B_{2g}	150.5	158.3	156.9
8	$\mathbf{E_{2g}}$	153.2	152.0	156.6
	E_{1u}			144.5
	E_{2u}			142.8
	B_{1u}			99.9
9	A_{2u}	105.2	88.3	95.0
	E_{1g}			84.3
10	E_{1u}	130.3	85.6	83.8
	A_{2u}			78.1
	E_{1u}			58.5

Table II. Optical Phonon Modes for distinct magnetic states, with frequencies in cm^{-1}. Modes listed in the last column only are the zone-boundary ($\mathbf{q} = (0, 0, 1/2)$) modes.

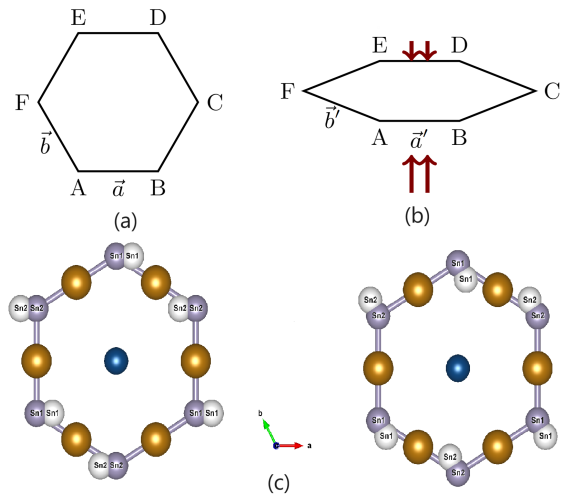

Figure 3. For a hexagonal lattice, (a) and (b) depict schematics for $\epsilon = 0$ and $\epsilon > 0$, respectively, illustrating symmetry reduction resulting from the application of unilateral strain. While the volume of the hexagonal crystal remains constant, the orientation of the hexagonal plane changes. Additionally, (c) showcases the doubly degenerate E_{2g} quadrupolar mode of the Sn (2d position) plane, with white balls indicating positions displaced due to the applied strain. The figures show the ab plane, while the c axis is perpendicularly out of the paper.

candidates, as shown in Table II in last column. Given the excellent agreement with the experiment for the E_{2g} mode, this strongly suggests that, if the observed satellites are from mode leakage, the leaking modes are from other points in the Brillouin zone.

On the other hand, while the observed satellite peaks are weaker than the main peak, their intensities are comparable. Leakage of forbidden modes requires a violation of the conservation of the quasi-momentum. One possibility for these are localized defects. Also, localized defects can lead to new local phonon modes that may be observable in Raman scattering. However, given that the intensities of these satellite peaks are comparable to the main peak, if these localized defects are the source of these satellite peaks, then either the concentration of such defects is strangely high, or the modes in question are exceptionally active. While neither is forbidden, it would be rather strange. To conclude, we do not have a convincing and natural explanation for the ubiquitous presence of these satellites.

In order to address possible magneto-phonon coupling, we have also calculated the Raman modes under the in-plane uniaxial volume-confirming strain. The latter reduces the symmetry to orthorhombic ($Cmmm$, #65), as shown schematically in Fig. 3. Note that while the compressive case in this case is not the same as the tensile strain, the difference arises only because the x (100) direction is not exactly equivalent to y (210) direction, and the difference is of the higher order in strain.

In Cartesian coordinates, a strain ϵ corresponds to the transformation matrix for the lattice vector of

$$\mathcal{R}' = \begin{pmatrix} (1+\epsilon) & 0 & 0 \\ -\frac{1}{2}(1+\epsilon) & \frac{\sqrt{3}}{2}\frac{1}{1+\epsilon} & 0 \\ 0 & 0 & 1 \end{pmatrix}.$$

This symmetry lowering opens up (quadratically in ϵ) Raman activity for previously inactive modes, as well as splits and shifts of the original E_{2g} mode. Specifically, the latter splits into an A_1g and a B_{1g} modes, and the original silent B_{2g} mode, corresponding to vertical shifts of the Sn_2 planes with respect to Fe_3Sn planes, becomes the B_{3g} Raman-active mode (Table III).

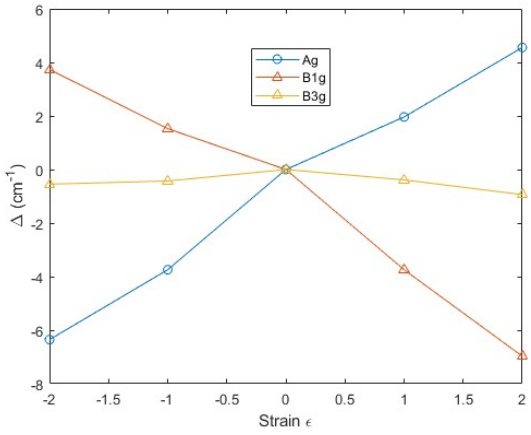

Figure 4. Change of selected zone-center phonons (for other modes, see the Supplementary Material) as a function of unilateral strain ϵ (in %) applied along the Fe-Fe bond. The notations are given as pertaining to the undistorted structure, i.e., the E_{2g} modes splits (linearly in ϵ) into A_g and B_{1g} (active in different polarizations) and the silent B_{2g} mode shifts (quadratically in ϵ) and acquires a Raman intensity proportional (also quadratically).

We observe that the strongest effect of strain is splitting of the main E_{2g} mode (Fig. 4). While the splitting per se is not observed experimentally, we see a shift of the central peak by ~ -1 cm^{-1}, consistent with the calculated shift for $\epsilon \approx 1\%$. We speculate that the higher-frequency component is not detected because of matrix elements. Notably, a reduction of about a factor of two in intensity occurs in the main peak (but not in the satellites), suggesting that the other half is silent in our geometry. The strain effects (at least this type of strain) cannot explain the presence of satellites for the following reasons: first, their frequencies differ from the main peak by 16 and 24 cm^{-1}, respectively, way too big to be associated to intrinsic strains in a free-standing sample. Second, the silent B_{2g} mode is only 2 cm^{-1} higher than the main peak and cannot be associated with the satellites. Third, internal strain is by nature inhomogenous, and that should make the strain-induced changes much broader than the central peak, which is not the case.

AFM coupling without strain		AFM coupling with Unilateral Strain				
Symmetry Species	Wave-Number (cm^{-1}) $\epsilon = 0$	Symmetry Species	Wave-Number (cm^{-1}) $\epsilon \rightarrow$	1%	−1%	2%	−2%
E_{2g}	156.6	A_g		158.6	152.9	161.2	150.3
E_{2g}	156.6	B_{1g}		152.9	158.1	149.6	160.4
B_{2g}	156.9	B_{3g}		156.5	156.5	156.0	156.3

Table III. Intensities for Raman active mode before and after the application of unilateral strain for antiferromagnetic magnetic pattern. The degenerate Raman active mode, E_{2g}, splits into A_g and B_{1g}, and the previously silent mode, B_{2g}, splits into Raman active mode B_{3g}.

IV. CONCLUSION

In conclusion, we measured Raman spectra on single crystals of antiferromagnetic kagome metal FeSn, in free form as well as in sample glued to a PET, with or without strain. We also performed first principle calculations on the same system, assuming different magnetic states for Fe: locally nonmagnetic, and ferro- or anti-ferromagnetically ordered. The central peak, corresponding to the Raman-active E_{2g} mode, is in excellent agreement with our calculation. Satellites of unknown origin were also observed. We can convincingly exclude internal strain or leakage of zone-center Raman-forbidden modes as the origin of these satellites. Localized impurity cannot be excluded, albeit we do not have any clear candidates, and the result appear to be reasonably sample-independent. The satellites are strong and sharp, and explaining their presence is an exciting challenge that future studies should meet.

We also find that suppressing the local magnetic moment on Fe leads to a considerable error in the phonon modes (up to 45 cm^{-1} in case of the E_{1u} mode, which is pure Fe). A similar effect was observed, for instance, in Ref. [34], but not on the same scale. Even more interesting, we find that the magnetic *order* couples strongly with some phonons, with up to 17 cm^{-1} shifts (in case of, unfortunately silent, E_{2u} mode). This is an exceptionally strong magneto-phonon coupling and may be related to the unusual kagome geometry.

Tuning of the band structure through strain engineering is central to semiconducting applications. It was theoretically proposed that bulk electronic states are reorganized by strain in the vicinity of the Dirac node and that strain breaks the degeneracy of edge states [35]. Recent reports suggested that strain induces periodic modulations of the Sn sublattice in thin films of FeSn grown on an $SrTiO_3$ substrate [36]. The modulations led to periodic differential conductance peaks, consistent with Landau levels generated by magnetic fields greater than 1000 Tesla [37]. Similarly, our observation of the strain-induced decrease of the E_{2g} mode intensity, associated with lateral Sn displacements, points to similar changes expected as in the epitaxially grown films. Furthermore, the strong Raman response under bending of the flexible substrate which is estimated to provide less than 1 % of tensile strain reflects the extreme sensitivity of the phonon modes. The drop in the intensity of the E_{2g} mode under strain indicates damping of the phonon mode with a small redshift. Strain changes the polarizability of the Sn π-orbitals thus reducing their contribution to the Raman signal. Layer dependence is another factor that can influence the intensity of Raman peaks, thus it is also possible that changes in the stacking order under strain can lead to our observations.

@Present address: Department of Chemical Engineering and Materials Science, University of Minnesota, Minneapolis, Minnesota 55455, USA

ACKNOWLEDGEMENTS

This work has been supported by the Department of Energy, Grant number DE-FG02-01ER4592. This work made use of instrumentation at the Nanoscale Materials Characterization Facility of University of Virginia.

[1] B. Keimer and J. Moore, Nature Physics **13**, 1045 (2017).
[2] E. Dagotto, Science **309**, 257 (2005).
[3] Y. Tokura, M. Kawasaki, and N. Nagaosa, Nature Physics **13**, 1056 (2017).
[4] D. Basov, R. Averitt, and D. Hsieh, Nature materials **16**, 1077 (2017).
[5] Z. Lin, J.-H. Choi, Q. Zhang, W. Qin, S. Yi, P. Wang, L. Li, Y. Wang, H. Zhang, Z. Sun, *et al.*, Physical review letters **121**, 096401 (2018).
[6] A. Kruchkov, Physical Review B **105**, L241102 (2022).
[7] N. Tilak, X. Lai, S. Wu, Z. Zhang, M. Xu, R. d. A. Ribeiro, P. C. Canfield, and E. Y. Andrei, Nature communications **12**, 4180 (2021).
[8] M. Kang, S. Fang, L. Ye, H. C. Po, J. Denlinger, C. Jozwiak, A. Bostwick, E. Rotenberg, E. Kaxiras, J. G. Checkelsky, *et al.*, Nature communications **11**, 4004 (2020).
[9] L. Ye, M. K. Chan, R. D. McDonald, D. Graf, M. Kang, J. Liu, T. Suzuki, R. Comin, L. Fu, and J. G. Checkelsky, Nature communications **10**, 4870 (2019).

[10] W. Song, Z. Yan, L. Ban, Y. Xie, W. Liu, J. Kong, W. Li, Q. Cheng, W. Xu, and D. Li, Physical Chemistry Chemical Physics **24**, 18983 (2022).

[11] S. A. Parameswaran, R. Roy, and S. L. Sondhi, Comptes Rendus Physique **14**, 816 (2013).

[12] K. Sun, Z. Gu, H. Katsura, and S. D. Sarma, Physical review letters **106**, 236803 (2011).

[13] M. Goerbig, The European Physical Journal B **85**, 1 (2012).

[14] Z. Liu and E. J. Bergholtz, arXiv preprint arXiv:2208.08449 (2022).

[15] T. Ito, H. Kumigashira, H.-D. Kim, T. Takahashi, N. Kimura, Y. Haga, E. Yamamoto, Y. Ōnuki, and H. Harima, Physical Review B **59**, 8923 (1999).

[16] Y. Xu, J. Zhao, C. Yi, Q. Wang, Q. Yin, Y. Wang, X. Hu, L. Wang, E. Liu, G. Xu, *et al.*, Nature communications **11**, 3985 (2020).

[17] M. Kang, L. Ye, S. Fang, J.-S. You, A. Levitan, M. Han, J. I. Facio, C. Jozwiak, A. Bostwick, E. Rotenberg, *et al.*, Nature materials **19**, 163 (2020).

[18] Y. Tao, L. Daemen, Y. Cheng, J. C. Neuefeind, and D. Louca, Physical Review B **107**, 174407 (2023).

[19] S.-H. Do, K. Kaneko, R. Kajimoto, K. Kamazawa, M. B. Stone, J. Y. Lin, S. Itoh, T. Masuda, G. D. Samolyuk, E. Dagotto, *et al.*, Physical Review B **105**, L180403 (2022).

[20] Y. Xie, L. Chen, T. Chen, Q. Wang, Q. Yin, J. R. Stewart, M. B. Stone, L. L. Daemen, E. Feng, H. Cao, *et al.*, Communications Physics **4**, 240 (2021).

[21] F. Theuss, S. Ghosh, T. Chen, O. Tchernyshyov, S. Nakatsuji, and B. Ramshaw, Physical Review B **105**, 174430 (2022).

[22] M. Ikhlas, S. Dasgupta, F. Theuss, T. Higo, S. Kittaka, B. Ramshaw, O. Tchernyshyov, C. Hicks, and S. Nakatsuji, Nature Physics **18**, 1086 (2022).

[23] W. Bazine, N. Tahiri, O. El Bounagui, and H. Ez-Zahraouy, Philosophical Magazine **102**, 1305 (2022).

[24] J. Liu, Z. Zhang, M. Fu, X. Zhao, R. Xie, Q. Cao, L. Bai, S. Kang, Y. Chen, S. Yan, *et al.*, Results in Physics **52**, 106803 (2023).

[25] L. Yin, D. Zhang, C. Chen, G. Ye, F. Yu, B. R. Ortiz, S. Luo, W. Duan, H. Su, J. Ying, *et al.*, Physical Review B **104**, 174507 (2021).

[26] G. Kresse and J. Hafner, Phys. Rev. B **47**, 558 (1993).

[27] G. Kresse and J. Furthmüller, Computational Materials Science **6**, 15 (1996).

[28] G. Kresse and J. Furthmüller, Phys. Rev. B **54**, 11169 (1996).

[29] H. Stokes, D. Hatch, and B. Campbell, "Smodes, isotropy software suite," (2021).

[30] H. T. Stokes and D. M. Hatch, Journal of Applied Crystallography **38**, 237 (2005).

[31] P. E. Blöchl, Phys. Rev. B **50**, 17953 (1994).

[32] J. P. Perdew, K. Burke, and M. Ernzerhof, Phys. Rev. Lett. **77**, 3865 (1996).

[33] R. T. Harley, J. B. Page Jr., and C. T. Walker, Phys. Rev. Lett. **23**, 922 (1969).

[34] D. Reznik, K. Lokshin, D. Mitchell, D. Parshall, W. Dmowski, D. Lamago, R. Heid, K.-P. Bohnen, A. Sefat, M. A. McGuire, *et al.*, Physical Review B **80**, 214534 (2009).

[35] T. Liu, Physical Review B **102**, 045151 (2020).

[36] H. Zhang, M. Weinert, and L. Li, Nano Letters **23**, 2397 (2023).

[37] C.-C. Hsu, M. L. Teague, J.-Q. Wang, and N.-C. Yeh, Science Advances **6**, aat9488 (2020).